JGR Space Physics

RESEARCH ARTICLE
10.1029/2023JA032360

A Statistical Survey of E-Region Anomalous Electron Heating Using Poker Flat Incoherent Scatter Radar Observations

Yizhe Zhang[1] and Roger H. Varney[2]

[1]School of Earth and Space Sciences, University of Science and Technology of China, Hefei, China, [2]Department of Atmospheric and Oceanic Sciences, University of California Los Angeles, Los Angeles, CA, USA

Key Points:

- A novel detection algorithm for identifying anomalous electron heating events primarily based on plasma flow velocities is presented
- Analysis of Poker Flat Incoherent Scatter Radar data from 2010 to 2023 detected 505 events
- Statistical analysis of occurrence rates revealed a strong relationship with geomagnetic activity over the 11-year solar cycle

Correspondence to:
R. H. Varney,
rvarney@atmos.ucla.edu

Citation:
Zhang, Y., & Varney, R. H. (2024). A statistical survey of E-region anomalous electron heating using Poker Flat Incoherent Scatter Radar observations. *Journal of Geophysical Research: Space Physics*, *129*, e2023JA032360. https://doi.org/10.1029/2023JA032360

Received 21 DEC 2023
Accepted 23 AUG 2024

Author Contributions:
Conceptualization: Roger H. Varney
Formal analysis: Yizhe Zhang
Methodology: Yizhe Zhang
Software: Yizhe Zhang
Supervision: Roger H. Varney
Writing – original draft: Yizhe Zhang
Writing – review & editing: Roger H. Varney

Abstract This work presents an algorithm for automatic detection of anomalous electron heating (AEH) events in the auroral E-region ionosphere using data from the Poker Flat Incoherent Scatter Radar (PFISR). The algorithm considers both E-region electron temperature and magnetically conjugate electric field measurements. Application of this algorithm to 14 years of PFISR data spanning 2010 through 2023 detected 505 AEH events. Measured electron temperatures increase linearly with plasma drift speeds. Statistical trends of AEH occurrence as a function of space weather indices (AE and F10.7) demonstrate correlations with the solar cycle and geomagnetic activity levels. The magnetic local time occurrence rates show preferences for dusk and dawn with most events in the dusk sector. Observed AEH events tend to appear in regions of relatively low electron density and do not appear inside intense auroral arcs with high electron density. Furthermore, AEH detection requires a higher electric field than predicted by the threshold for a positive growth rate of the Farley-Buneman instability (FBI), according to linear fluid theory. The implications of these findings for kinetic theories of FBI and AEH are discussed.

Plain Language Summary The ionized portion of the upper atmosphere, known as the ionosphere, can conduct electrical currents. In cases where those currents are so large that the relative motion of the electrons and ions exceeds a critical threshold, the ionosphere becomes unstable. The resulting instability rapidly heats electrons in the lower ionosphere, producing what are known as anomalous electron heating (AEH) events. We use ionospheric data from a radar facility in Alaska to detect AEH events. Our detection algorithm identified 505 AEH events in 14 years of data (2010–2023). The occurrence rates of AEH are strongly correlated with the 11-year solar cycle and indicators of auroral activity. Furthermore, AEH events preferentially occur at times near dawn and dusk, with the highest number of events in the dusk sector. The elevated electron temperatures increase linearly with the magnitude of the ionospheric electric field.

1. Introduction

In the lower ionosphere collisions with the neutral gas deflect charged particle drifts away from the $\mathbf{E} \times \mathbf{B}$ drift direction, and the differing deflections for ions and electrons results in net current flowing perpendicular to the geomagnetic field (Chapman, 1956). If the currents are sufficiently strong, the electron-ion velocity difference can exceed the threshold for the modified two-stream instability (MTSI), also known as the Farley-Buneman instability (FBI) (Buneman, 1963; Farley, 1963). The FBI was originally investigated as an explanation for plasma irregularities in the equatorial electrojet (EEJ), a region of intense current in the daytime equatorial ionosphere (Farley, 1963; Yamazaki & Maute, 2017). Radars looking perpendicular to the geomagnetic field can detect coherent scatter from plasma irregularities if the density irregularities meet the Bragg scattering condition (Sahr & Fejer, 1996). The original study of FBI by Farley (1963) hypothesized this instability to explain coherent scatter observations in the EEJ.

At auroral latitudes radars can observe coherent scatter from a variety of different plasma irregularities when looking perpendicular to the geomagnetic field. FBI is theorized to be the primary source of "Type 1" radar echoes, which are coherent scatter echoes with very narrow spectral widths and phase velocities near the ion-acoustic speed (Sahr & Fejer, 1996). Auroral arcs carry large field-aligned currents between the magnetosphere and ionosphere, and these currents need to close horizontally through the ionosphere. The FBI instability should be triggered when these horizontal currents become large enough to exceed the instability threshold. Radar imaging studies in coordination with optical observations of the aurora show that regions of coherent scatter

appear immediately adjacent to optical auroral arcs, but not inside the brightest auroral arcs (Bahcivan et al., 2006; Huyghebaert et al., 2021). These observations are consistent with the strongest electric fields and the most unstable plasma appearing adjacent to auroral arcs where horizontal currents are forced to close through relatively lower conductivity regions of the ionosphere.

In addition to coherent scatter echoes, FBI can also be indirectly observed by incoherent scatter (IS) radars by looking for anomalous electron heating. IS radars observe the weak scatter from the thermal distribution ionospheric electrons, and they do not require the existence of irregularities or an observation geometry perpendicular to **B**. Incoherent scatter theory (Kudeki & Milla, 2011) predicts the scattering power and scattering spectrum based on the electron density, electron temperature, ion temperature, and ion line-of-sight velocity. IS radars routinely measure altitude profiles of these four parameters. Usually the E-region electron temperatures between 90 and 130 km altitude nearly matches the neutral temperature profile (250–400 K). The Chatanika Radar in Chatanika, Alaska was the first to record instances of unusually elevated E-region electron temperatures in a narrow altitude range (Schlegel & St.-Maurice, 1981). These anomalous electron heating (AEH) events have subsequently been observed by the European Incoherent Scatter Scientific Association (EISCAT) radars in Tromsø, Norway (Saito et al., 2001), the Sondrestrom Radar in Sondrestromfjord, Greenland (Milikh et al., 2006), the Poker Flat Incoherent Scatter Radar (PFISR) in Chatanika, Alaska (Makarevich et al., 2013), and the Resolute Bay Incoherent Scatter Radar (RISR) in Resolute Bay, Canada (St-Maurice & Goodwin, 2021). AEH observations made by IS radars are always made at observation angles very far away from perpendicular to **B** where the Farley-Buneman waves will not meet the Bragg scattering condition required to create coherent scatter returns.

The current theory of AEH explains the extreme electron heating rates required by invoking the nonlinear dissipation of Farley-Buneman waves. AEH appears at low altitudes in the E-region ionosphere where inelastic collisions with neutrals, especially collisions that excite the vibrational states of N_2, are efficient at cooling the electron gas (Schunk & Nagy, 2009). AEH therefore requires large and persistent electron heating to maintain the elevated electron temperatures. St.-Maurice et al. (1981) theorized that FBI would saturate nonlinearly and dissipate by heating electrons. Subsequent work highlighted the need for turbulent parallel electric fields to form during the nonlinear saturation process in order to explain the efficient energy transfer to the electrons (St.-Maurice & Laher, 1985). Particle-in-cell (PIC) simulations of FBI show that the waves saturate non-linearly, produce turbulent parallel electric fields, and dissipate energy by heating the electrons (Dimant & Oppenheim, 2011a, 2011b; Oppenheim & Dimant, 2013).

Interest in FBI and AEH has recently expanded because these small-scale instabilities may have feedback effects on the global-scale electrodynamics and magnetosphere-ionosphere coupling. PIC simulations demonstrate that the nonlinear dissipation scatters electrons away from the $\mathbf{E} \times \mathbf{B}$ drift direction, resulting in anomalous electron mobility and increased Pedersen conductivity (Dimant & Oppenheim, 2011b). Additionally, the elevated electron temperatures caused by AEH will slow down chemical recombination rates. The most important recombination processes in the E-region ionosphere are dissociative recombination molecular ions, especially NO^+ and O_2^+, and the dissociative recombination rates decrease with increasing electron temperature (Milikh et al., 2006). Decreased recombination rates will increase the equilibrium electron density, resulting in higher ionospheric conductivity. The combined effects of the anomalous electron mobility and the decreased recombination rates should raise the ionospheric conductivity in FBI unstable regions (Dimant & Oppenheim, 2011b). Including these effects turns the high-latitude ionospheric electrodynamics problem into a nonlinear problem where the ionospheric conductivity depends on the electric field magnitude.

An ongoing challenge in geospace research is the parameterization and inclusion of FBI effects into regional and global geospace models (Liu et al., 2016; Merkin et al., 2005). Ionospheric conductivity determines the inner-boundary condition for magnetospheric currents, and these boundary conditions will effect the entire magnetospheric solution in global coupled models (Lotko et al., 2014). Correctly quantifying the impact of nonlinear ionospheric conductivity on the coupled geospace system crucially depends on accurate predictions of when and where FBI should occur in a global ionospheric solution. For this reason, recent work has carefully re-examined the instability thresholds. Dimant et al. (2021) proposed that kinetic theory predicts a considerably higher instability threshold than fluid theory in the presence of energetic electrons from particle precipitation since the energetic electrons can more efficiently dissipate energy through inelastic collisions with N_2.

This paper aims to expand the empirical knowledge of when and where AEH occurs in the hopes that these statistics can help constrain and validate future model parameterizations of nonlinear conductivity. This paper analyzes 14 years of nearly continuous PFISR E-region observations covering 2010–2023, making it the longest systematic survey of AEH yet conducted and the first to cover more than a full solar cycle of observations. The previous work by Makarevich et al. (2013) only considered PFISR observations from 2010 to 2011, which were years of low to moderate activity at the beginning of solar cycle 24. Section 2 explains the data sources and Section 3 describes our analysis methods and AEH detection algorithms. Section 4 summarizes our statistical results, Section 5 discusses the ramifications of our results, and Section 6 summarizes our conclusions.

2. Data Sources

The data utilized in this study were primarily sourced from the PFISR, which is an Advanced Modular Incoherent Scatter Radar (AMISR) system located at Poker Flat Research Range (65.13°N, 147.47°W, MLAT = 65.4°N) in Chatanika, Alaska. Our data set encompasses all data between January 2010 and July 2023 that was published in the SRI International AMISR database as of August 2023. PFISR began its operations in 2007; hence, our data set covers a significant majority of the operational timeline of PFISR, ensuring a robust and extensive basis for our analysis.

We exclusively utilized two types of processed files for our study: the alternating code files and the vector velocities files. While PFISR employs a variety of different experimental modes, most experiments include pulses dedicated to E-region measurements using a 480 μs 16-baud randomized strong alternating code (Lehtinen et al., 1997), oversampled at 10 μs and processed into decoded autocorrelation functions with fractional-lag processing (Huuskonen et al., 1996). The fitted alternating code files provide measurements of electron density, electron and ion temperatures, and line-of-sight velocities. Additionally, the alternating code files also include model-based calculations of the background magnetic field and ion-neutral collision frequencies of different species based on neutral densities from the Naval Research Laboratory Mass Spectrometer and Incoherent Scatter (NRLMSISE-00) model (Picone et al., 2002). The alternating code fitting uses a steady-state ion chemistry model to solve for the molecular ion composition consistent with the fitted electron density and ion temperature (Richards et al., 2009), and the alternating code files include the modeled ion fractions.

The vector velocity processed files are the output of the Heinselman and Nicolls (2008) electric field and F-region vector velocity reconstruction algorithm. This algorithm uses fitted line-of-sight velocities from F-region altitudes sampled by uncoded long pulses and reconstructs vector velocities as a function of magnetic latitude assuming the F-region drifts are dominated by the $\mathbf{E} \times \mathbf{B}$ drift, electric fields map along equipotential field lines, and the drifts are uniform in the magnetic east-west direction. Our evaluation of instability thresholds uses electric field data extracted from the vector velocities files.

Essentially all PFISR experiments exploit the electronic beam steering capability of the radar to sample multiple beams, and different experimental modes have different selections of beams. Our detection of AEH is based on alternating code electron temperature at 110 km since this is the altitude with the largest rate of increase in T_e with electric field (see slopes in Table 1 of St-Maurice and Goodwin (2021)). Our electric field data is derived from F-region measurements that are not in a common volume. Nonetheless, we can assume electric fields map along equipotential field lines and match E-region measurements with magnetically conjugate electric field measurements. The electric field data typically has the smallest errors in the latitude bins between 66.0 and 66.5° of magnetic latitude for most PFISR beam geometries, so we selected beams from the alternating code data where the range gate at 110 km maps to approximately 66.0°. Below 66.0° the F-region lines of sight are too close to parallel to $\mathbf{B}$ to derive reliable estimates of the $\mathbf{E} \times \mathbf{B}$ drift. Each beam is assigned a 16-bit beamcode. Our analysis searches for the first beamcode in Table 1, in that order. Beamcodes 64067, 64055, or 64052 map to electric field data from the 66.25° latitude bin, and the others map to electric field data from the 66.0° latitude bin, as is shown in the last column of Table 1. Almost all experiment use at least one of these beamcodes. Note that we are not using the beam position parallel to $\mathbf{B}$ because there is no way to map that beam to magnetically conjugate electric field information.

The PFISR data set encompasses files with various time resolutions. Particularly in Themis mode, it is common for the alternating code file and the vector velocity file to be available in disparate time resolutions. To synchronize values across both files, it is necessary to standardize them to a shared time resolution. This is accomplished by first applying a moving median to the file with the higher resolution, typically the vector velocity

Table 1
The Selected Beamcodes and the Corresponding Azimuth Angles, Elevation Angles, and the Magnetic Latitude of the Chosen Electric Field Data

Beamcode	Azimuth (degrees)	Elevation (degrees)	E magnetic latitude (degrees)
64067	20.50	58.00	66.25
64055	20.50	64.00	66.25
64052	20.50	66.00	66.25
65066	75.03	65.56	66.0
63239	−16.23	58.68	66.0
63401	57.23	58.68	66.0
64343	96.50	55.86	66.0
64919	−28.80	70.09	66.0

file, to smooth it. Utilizing the timestamps from the lower-resolution file, we locate the temporally nearest smoothed values from the higher-resolution file. A new file is then assembled using these values and their respective timestamps, ensuring it maintains the same time resolution as the lower-resolution file. The newly constructed file is then used in subsequent analyses and calculations.

For instances where data files are available in multiple time resolutions, we opt for the highest resolution, excluding the 1 and 1.5 min resolutions. This is typically 3 min in Themis modes and 5 min in IPY modes. Unless no other time resolutions are available, we avoid 1 and 1.5 min resolutions as these files often contain significant errors due to their finer granularity. In contrast, the 3 and 5 min resolution files strike an optimal balance, especially suitable for detecting AEH and analyzing their temporal correlations. Due to significant discrepancies between electron temperature and electric field data in some files, our program takes further measures to mitigate errors in the data set. Electric field data exhibiting errors greater than 10 mV/m are excluded.

As shown in Figure 1, the coverage of the data we ultimately used in this study over 14 years is 3,396 days (obtained by summing the coverage time of all files), which is approximately 66% of 14 years. There are significant gaps in the PFISR data during two time intervals: 2014–2016 and in 2022. These gaps are the result of unprocessed or unpublished intervals in the SRI International AMISR database. Nonetheless, this data coverage is sufficient to study the statistical trends of AEH occurrence over a complete solar cycle.

3. Analysis

We developed an "instability index" based on the linear growth rate of the FBI to predict the occurrence of AEH. We show that the instability index maintains a close, positive relationship with the electric field mapped in the E-region, which, in turn, positively correlates with the anomalously heated electron temperature. However, when we tried to use the linear theory and our "instability index" to identify AEH events in observations, we found thousands of instances where AEH did not occur as predicted by the linear theory. After a comprehensive statistical analysis, we determined that AEH usually appears at flow velocities over 1,000 m/s, which is higher than the threshold velocity for FBI predicted by linear theory. The Appendix A provides further details on this analysis.

In order to make our instability index consistent with observations, we multiplied the index with a hyperbolic tangent function term to eliminate events with insufficient flow velocities. The modified index will be referred to as "modified instability index" in the following text. We then formulate a new strategy for AEH identification primarily relying on the "modified instability index." Our novel algorithm has proven superior to one based solely on electron temperature. Utilizing this new approach, we have acquired a larger and more comprehensive AEH data set, comprising 505 events. Applying this enhanced data set, we analyze the relationship between electron temperature and plasma flow velocity, deriving a linear result analogous to that obtained by St-Maurice and Goodwin (2021).

3.1. Linear Fluid Theory and Instability Index

The FBI typically develops in regions where the relative velocity between electrons and ions approaches or even exceeds the isothermal sound speed C_s, given by

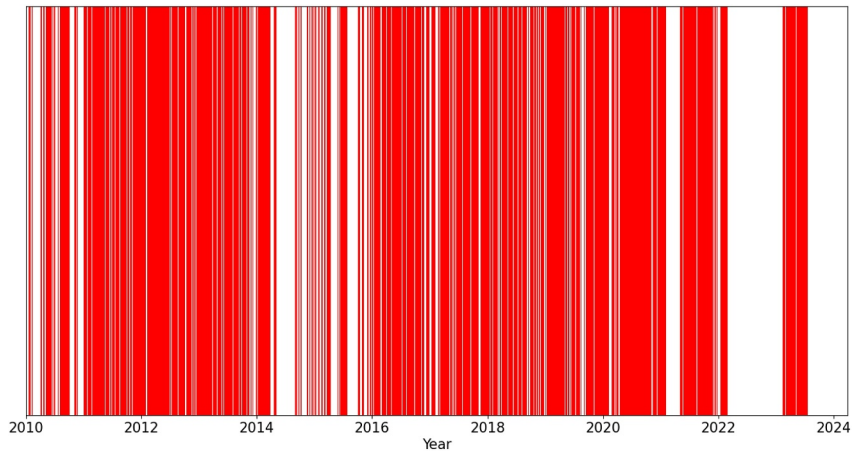

Figure 1. This figure shows the temporal coverage of the data we used. The red bars represent the periods covered by data, and the width of the bars indicates the duration of data coverage. The horizontal axis represents the years.

$$C_s = \sqrt{\frac{k_B(T_e + T_i)}{m_i}} \tag{1}$$

where k_B is Boltzmann's constant, T_e and T_i are the electron and ion temperatures, and m_i is the ion mass. For NO^+ plasma with $T_e = T_i = 300$ K this speed is approximately 400 m/s. In the E-region, spanning altitudes from 90 to 120 km, electrons are generally governed by the magnetic field, exhibiting a significantly large gyro-frequency and a relatively small collision frequency $\left(\Omega_e = \frac{eB}{m_e} \gg \nu_{en}\right)$. In contrast, ions, due to their substantial mass, possess a smaller gyro-frequency comparable in magnitude to the collision frequency $\left(\Omega_i = \frac{eB}{m_i} \approx \nu_{in}\right)$. Consequently, ions deviate from their original state of motion due to collisions with neutral particles, while electrons undergo $\mathbf{E} \times \mathbf{B}$ drift $(V_e \approx E_\perp / B)$. The magnitude of the relative velocity between electrons and ions is essentially the $\mathbf{E} \times \mathbf{B}$ drift velocity minus ion velocity. Here, "perpendicular" and "parallel" are both in relation to the background magnetic field. An electric field exceeding 30 mV/m, which is a common phenomenon in the auroral oval, corresponds to an $\mathbf{E} \times \mathbf{B}$ drift velocity of 600 m/s. The electron-ion relative velocity will be less than the $\mathbf{E} \times \mathbf{B}$ drift velocity, depending on the altitude. When the relative velocity exceeds the ion acoustic velocity, the FBI is likely to manifest, potentially leading to an AEH event.

According to linear theory, when considering fully magnetized electrons and partially magnetized ions, the real and imaginary parts of the dispersion relation for Farley-Buneman waves can be expressed as (Dimant & Milikh, 2003):

$$\omega_k = \frac{\mathbf{k} \cdot \left[\mathbf{V}_{e0} + \psi\left(1 + \kappa_i^2\right)\mathbf{V}_{i0}\right]}{1 + \psi\left(1 + \kappa_i^2\right)} \tag{2}$$

$$\gamma_k = \psi \frac{\left(1 - \kappa_i^2\right)(\omega_k - \mathbf{k} \cdot \mathbf{V}_{i0})^2 - k^2 C_s^2}{\nu_{in}\left[1 + \psi\left(1 + \kappa_i^2\right)\right]} \tag{3}$$

The parameter κ is defined as the ratio of a species' gyro-frequency to its collision frequency.

$$\kappa_i = \frac{\Omega_i}{\nu_{in}}, \qquad \kappa_e = \frac{\Omega_e}{\nu_{en}} \tag{4}$$

The dimensionless parameter ψ relates to the collisional damping of Farley-Buneman waves. By assuming that the wave vector is quasi-perpendicular to the background magnetic field $\left(k_\perp \gg k_\parallel\right)$, we can make an approximation for ψ as follows:

$$\psi = \psi_{\perp}\left(1 + \frac{k_{\parallel}^2 \Omega_e^2}{k_{\perp}^2 \Omega_i^2}\right) \approx \psi_{\perp} \tag{5}$$

$$\psi_{\perp} = \frac{1}{\kappa_e \kappa_i} = \frac{\nu_{en}\nu_{in}}{\Omega_e \Omega_i} \tag{6}$$

Upon substituting the wave frequency ω_k into Equation 3 and simplifying the growth rate expression, we observe that since the remaining parts of the expression are all positive, a positive numerator will result in a positive overall growth rate, indicating the presence of instability.

$$\gamma_k = \psi k^2 C_s^2 \frac{\frac{\left(1-\kappa_i^2\right)\left(\mathbf{k}\cdot\left(\mathbf{V}_{e0}-\mathbf{V}_{i0}\right)\right)^2}{\left(1+\psi\left(1+\kappa_i^2\right)\right)^2 k^2 C_s^2} - 1}{\nu_{in}\left[1+\psi\left(1+\kappa_i^2\right)\right]} \tag{7}$$

The wave vectors **k** are not observable from PFISR data. However, if we assume that the wave vector of the fastest growing modes are parallel to the relative velocity of electrons and ions—an assumption holding true in most cases—we can eliminate it from the expression. Consequently, the condition for instability is as follows:

$$\sqrt{\left(1-\kappa_i^2\right)}\ \frac{\left|\mathbf{V}_{e0}-\mathbf{V}_{i0}\right|}{\left(1+\psi\left(1+\kappa_i^2\right)\right)C_s} > 1 \tag{8}$$

We designate the left term as the "original instability index," denoted as OII. An OII greater than one indicates a positive growth rate, signifying the occurrence of FBI.

$$OII = \sqrt{\left(1-\kappa_i^2\right)}\ \frac{\left|\mathbf{V}_{e0}-\mathbf{V}_{i0}\right|}{\left(1+\psi\left(1+\kappa_i^2\right)\right)C_s} \tag{9}$$

The factor $\sqrt{\left(1-\kappa_i^2\right)}$ indicates that there exists a cutoff of OII at the height where $\kappa_i = 1$. Observationally, the typical value for this height is approximately 120 km or below. Observations of AEH above 120 km are exceedingly rare, which is consistent with fluid theory.

Substituting this expression for OII back into the expression for the growth rate reveals that the growth rate of the FBI is positively correlated with OII. Thus, it can be inferred that a higher OII signifies stronger instability, increasing the likelihood of AEH events.

$$\gamma_k = \left(OII^2 - 1\right)\frac{\psi k^2 C_s^2}{\nu_{in}\left[1+\psi\left(1+\kappa_i^2\right)\right]} \tag{10}$$

3.2. The Modified Instability Index

We calculate the OII as a function of altitude and time using the reconstructed electric field data in PFISR's velocity vector files and additional information in PFISR's alternating code files. We assume V_{e0} is the $\mathbf{E}\times\mathbf{B}$ drift and that electric field maps along the field line. The κ_i factors are computed from the NRLMSISE-00 collision frequencies in the alternating code files. The V_{i0} is computed from the electric field and the κ_i factors by solving the perpendicular momentum equation ignoring the neutral wind. The effective ion velocity is a weighted sum over all ion species, weighted by the number density fractions, $f_i = N_i/N_e$, determined by the chemistry model in the AMISR fitter.

$$\mathbf{V}_{i0} = \sum_i f_i \left\{\frac{\kappa_i}{1+\kappa_i^2}\frac{\mathbf{E}}{B} + \frac{\kappa_i^2}{1+\kappa_i^2}\frac{\mathbf{E}\times\mathbf{B}}{B^2}\right\} \tag{11}$$

Comparing the calculated OII with the observed electron temperature at altitudes of 100–120 km, we find that a positive growth rate according to fluid theory ($OII > 1$) is indeed a necessary, but not sufficient, condition for

AEHs. This implies that observed AEH events are invariably accompanied by a positive growth rate ($OII > 1$), yet a situation where $OII > 1$ does not necessarily indicate that an AEH is occurring. In fact, our analysis reveals that the condition $OII > 1$ is satisfied much more frequently than AEH is observed. Given the rarity of AEH, this finding also implies that there are numerous instances when the linear growth rate is positive ($OII > 1$), yet no AEH occurs. In these situations the FBI is either suppressed by mechanisms unexplainable by fluid linear theory, or it is too weak to generate sufficiently large electron heating to be detectable by PFISR. Therefore the OII alone is not an effective basis for an AEH detection algorithm. We then tried to modify our OII to make it corresponds better with AEH events.

Similar to the Makarevich et al. (2013) algorithm, we designed an electron temperature based algorithm and successfully detected a subset of AEH events and "suppressed events." We found that the distribution of those events on the flow velocity-electron density plane formed into two clusters. The two clusters are divided by a "separation value" of a flow velocity of 1,000 m/s. A large majority of the detected AEHs (using the electron temperature based algorithm) possesses a flow velocity larger than 1,000 m/s, while the flow velocity of most of the suppressed events is less than the value. We believe that our instability index can be improved by including this value into it, as this value serves as a compromise between including more "suppressed events" and generating more true results. Detailed information on the detection algorithm used and the reasoning of the inclusion is included in Appendix A.

Two example events are illustrated in Figure 2. The time period highlighted by the white box are AEH events identified. It is evident that the calculated OII remains greater than one for several hours, while there is a brief period of AEH lasting no more than half an hour. These events typically exhibit relatively large flow velocities (greater than 500 m/s), accounting for the positive linear growth observed during such events. From the last row in Figure 2, it can be clearly seen that only when the flow velocity approaches 1,000 m/s will AEH happen.

We construct our modified instability index (MII) by scaling the OII by a smoothly varying hyperbolic tangent function such that the MII is 0 if the flow velocity is less than 1,000 m/s and the MII equals the OII if the flow velocity becomes larger than 1,000 m/s. The expression for the new modified instability index is as follows:

$$MII = OII \cdot \frac{1}{2}\left[\tanh\left(0.1 \cdot \left[\frac{E_\perp}{B} - 1000\right]\right) + 1\right] \tag{12}$$

Multiplying the quantity in the hyperbolic tangent function by 0.1 is to make its function value change from zero to one more smoothly. The flow speed now needs to increase by 20 m/s for its function value to approach 1 from 0. Changing this transition factor only influences the detection result in a very limited way. Hence, every point that satisfies $MII > 1$ will have a positive growth rate ($OII > 1$) and a flow velocity bigger than 1,000 m/s.

By comparing the second row and the third row in Figure 2, which represents MII values and OII values respectively, we can easily find that the MII corresponds very well to AEH events, while OII seems to be bigger than one for several hours even when there was no AEH happening. Besides those two typical events shown in Figure 2, we have sufficient evidence suggesting a very close relation between AEH events and $MII > 1$, which is discussed in Appendix A. Therefore, we decided to use a new AEH detection algorithm based mainly on the MII condition. Due to the fact that the MII is mostly dependent on flow velocity, our new algorithm is primarily based on flow velocity instead of electron temperature.

Both preceding studies and our observational work corroborate that AEH events are highly likely to occur under $\frac{E_\perp}{B} > 1000$ m/s, and the FBI is seldom suppressed under this condition. This implies that the results of our new algorithm are likely to contain very few false positive events. Nonetheless, owing to the unavoidable errors in the electric fields and electron density data, we establish a relatively lenient criterion $T_e > 450$ K on temperature to exclude those inaccuracies. 450 K is only 50 K above the typical electron temperature value, yet this condition has proven to be highly efficient in eliminating measurement errors.

According to the empirical formula for the temperature-velocity relationship at 110 km derived by St-Maurice and Goodwin (2021),

$$T_e = 1.57\frac{E_\perp}{B} - 1057 \tag{13}$$

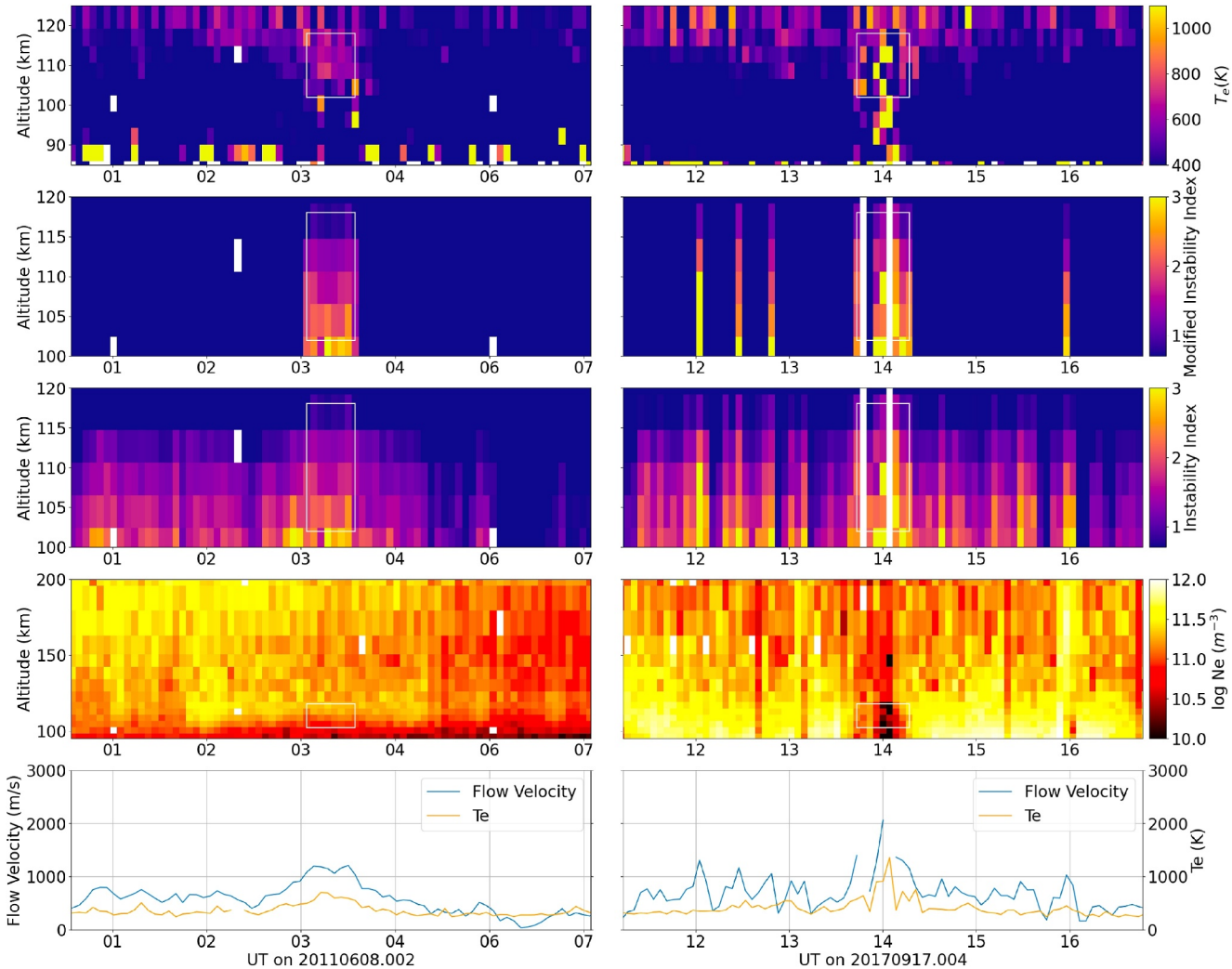

Figure 2. This figure presents two representative events that are detected by our flow velocity based algorithm. Additionally, they are typical examples of suppressed events. Each event is depicted through five subfigures, representing electron temperature, MII, OII, electron density, and flow velocity respectively.

the electron temperature should exceed 513 K when the flow velocity exceeds 1,000 m/s. Therefore the $MII > 1$ criterion should be able to detect AEH events from 513 K.

In conclusion, our novel detection strategy is primarily based on plasma flow velocity. It is composed of two conditions: $MII > 1.1$ and $T_e > 450$ K. The former will identify points with large flow velocity and positive linear growth rate. The latter serves as a relatively relaxed criterion established for the purpose of eliminating observational errors. This algorithm is referenced as algorithm 4 in Table A1 in Appendix A.

3.3. Detection Algorithms

The two conditions listed above are still inadequate to automatically detect AEH. AEH events always exhibit variations, whether significant or minor, in temperature and flow speed. Only a very few events truly meet the criteria at every single point. Thus, for such variations, our algorithm should consider them as a whole detected AEH event, rather than excluding these fluctuations. Here, we should also mention that these variations naturally result in certain segments of detected AEH having temperatures or flow speeds below our set detection standards. This will be reflected in our results in the following text.

Therefore, our algorithm should be separated into two parts. The first part involves identifying "anomaly data points" within data sets. Here, a data point represents the value of certain parameters at a specific time and

altitude, visualized as a point in a 2D contour plot. Points are classified as anomaly data points if they satisfy the set criteria. In this case, the criterion is $MII > 1.1$ and $T_e > 450$ K. The second part of the algorithm performs temporal correlation analysis on these anomaly data points to reject transient outliers.

Regarding the temporal correlation analysis, the criteria are delineated as follows:

1. Adjacent points with index intervals smaller than a critical value N_1 will be identified as sequential points.
2. A group of sequential points must encompass at least N_2 points.
3. Two sets of sequential points separated by an interval less than 30 min will be identified as a single group.

A group that meets the above three conditions will be ultimately identified as an AEH event. The critical values N_1 and N_2 are enumerated in Equation 14. The term max(10/res,3) denotes the maximum of the two values, where "res" denotes the time resolution of an alternating code file in minutes.

$$N_1 = \max(10/res, 3)$$
$$N_2 = \max(4, \min(20/res, 6)) \quad (14)$$

We have aimed to align our critical value with the parameters described in Makarevich et al. (2013). The critical value, N_1, stipulates that for an alternating code (ac) file with a time resolution of 5 min or longer, adjacent data points should have time intervals no greater than 15 min or three times the time resolution. For those with a time resolution of 3 min or less, the interval must not exceed 10 min. These parameters comparable to Makarevich's criteria for the median time between successive points: 15 min for the 5-min resolution IPY mode and 10 min for all Themis modes.

Regarding N_2, it mirrors Makarevich's prerequisites for the cumulative anomalous points within an AEH event: 5 for the 5-min resolution IPY mode and 3 for all Themis modes. In a similar vein, N_2 ensures that a detected AEH event comprises more than 4 anomalous points when its time resolution is 5 min or longer. For a time resolution of 3 min or less, the event must contain at least 6 anomalous points.

Because of the temporal correlation analysis, an event is identified as AEH as long as there are a few temporally correlated points that meet the detection criteria, not necessarily all points within the event.

3.4. AEH Detection Based on Modified Instability Index

A total of 505 AEH events have been identified through the new algorithm spanning 2010–2023. Due to the relaxed criteria on electron temperature, our algorithm is adept at detecting a greater number of AEH events, even those characterized by relatively low electron temperature and weak temporal correlation. We manually went over all the 505 results detected by algorithm 4 and only found 18 questionable events that we would not have necessarily classified as AEH by visual inspection. We retained these questionable events in our statistical analysis, but they are such a small portion of the data set that they have an insignificant effect on our conclusions.

In order to evaluate the performance of the algorithm, we compare its results to a control group. Our new algorithm is proven to be better than an electron temperature based algorithm. The detailed information is in Appendix A. In short, the new algorithm is capable of detecting weak events and generates fewer false positives. It is less impacted by the measurement error on electron temperature, and it contains less ambiguous events whose heating mechanisms are difficult to tell even by human inspection. Finally, its result shows a more pronounced linear relationship between electron temperature and flow velocity.

Figure 3 shows two typical AEH events with strong temporal correlation and enhanced electron temperature. Examining the second and third rows from the top in Figure 3, which present 2D plots of MII and OII respectively, it is evident that MII holds a significant advantage over OII in correlating with AEH events. In the majority of our 505 events, MII consistently exhibits a stronger correlation to AEH events compared to OII. This indicates that in real-world scenarios the threshold based on linear fluid theory is insufficient to predict AEH.

4. Statistics

In this section, we will perform statistical analysis on the detection results. We first analyze the distributions of events in the space of electron density, flow velocity, and electron temperature (N-V-T space). We then compare

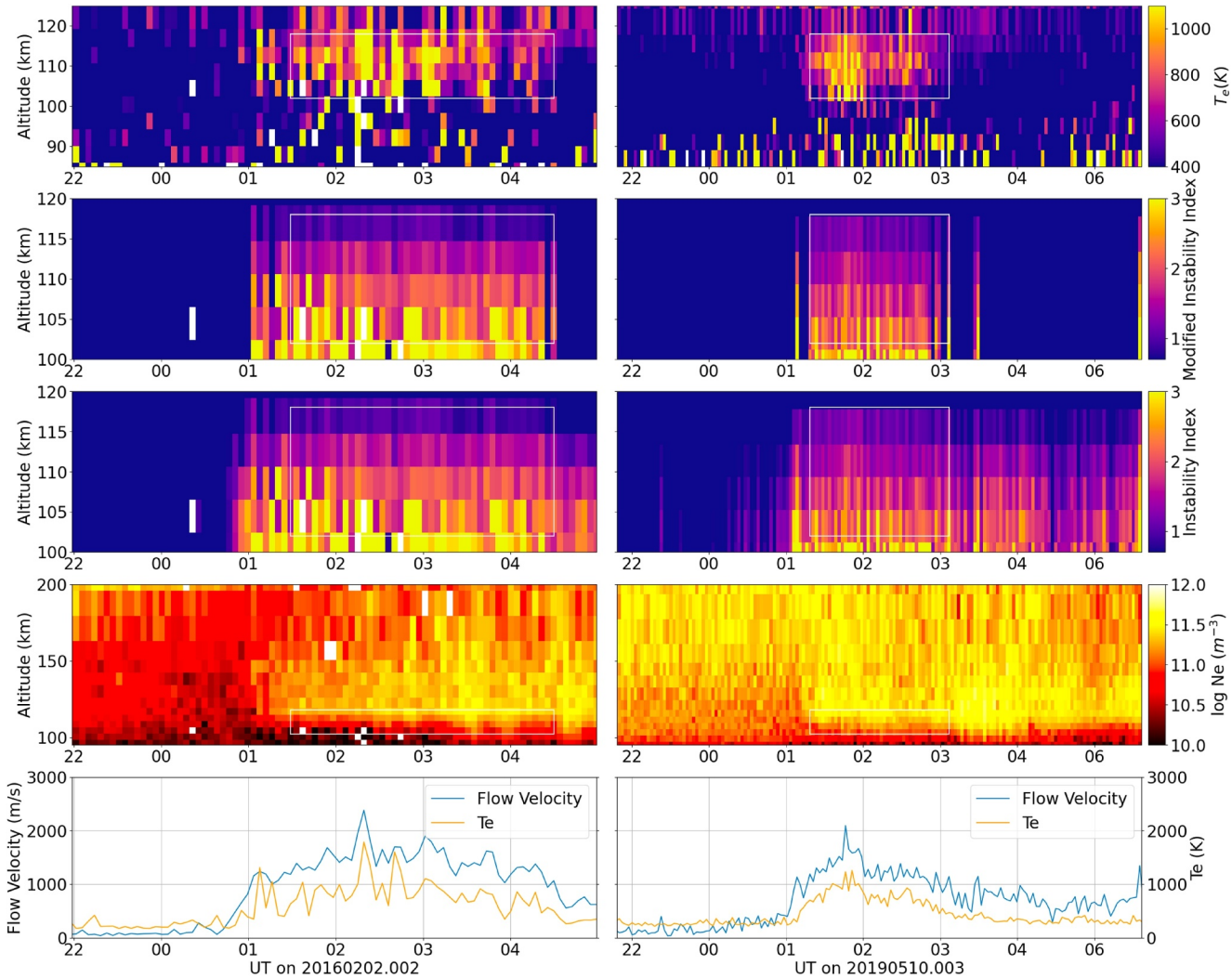

Figure 3. This illustration displays two exemplary AEH events, encased within the white solid lines. Each column, descending from the top, respectively represents the electron temperature plot, MII plot, OII plot, electron density plot, and a correspondence plot of flow velocity and electron temperature at 110 km. The horizontal axes across all panels represent Universal Time (UT).

the occurrence count and frequency of AEH events to the long-term variations of the AE index and the F10.7 index. Based on this comparison, we will highlight a strong correlation between AEH events, geomagnetic activity, and solar activity. Furthermore, our observations reveal that AEH events predominantly occur in the dawn and dusk sectors and exhibit a seasonal preference, being more frequent in summer than in winter.

4.1. Density, Velocity, and Temperature Relationships

Figure 4 showcases the distribution of AEH events in N-V-T space by showing scatter plots of N-V, N-T, and T-V. The distribution along the Y-direction in panels (a) and (b), both representing $\log_{10}N_e$, distinctly indicates that, unlike suppressed events, AEH events tend to occur at a typical electron density near $10^{11}\mathrm{m}^{-3}$. They are unlikely to occur at either extremely high density of $10^{11.5}\mathrm{m}^{-3}$ or extremely low density of $10^{10.25}\mathrm{m}^{-3}$.

Panels (a), (b), and (c) all exhibit a linear relationship between electron temperature and plasma flow velocity, which is consistent with prior studies (St-Maurice & Goodwin, 2021). From the last row in Figure 3, a strong correlation is observable between flow velocity and electron temperature, indicating a close relationship between the two parameters. Furthermore, the 2D histograms in panels (c) and (d) suggest a linear relationship between these two parameters, with the majority of the points clustering near a straight line.

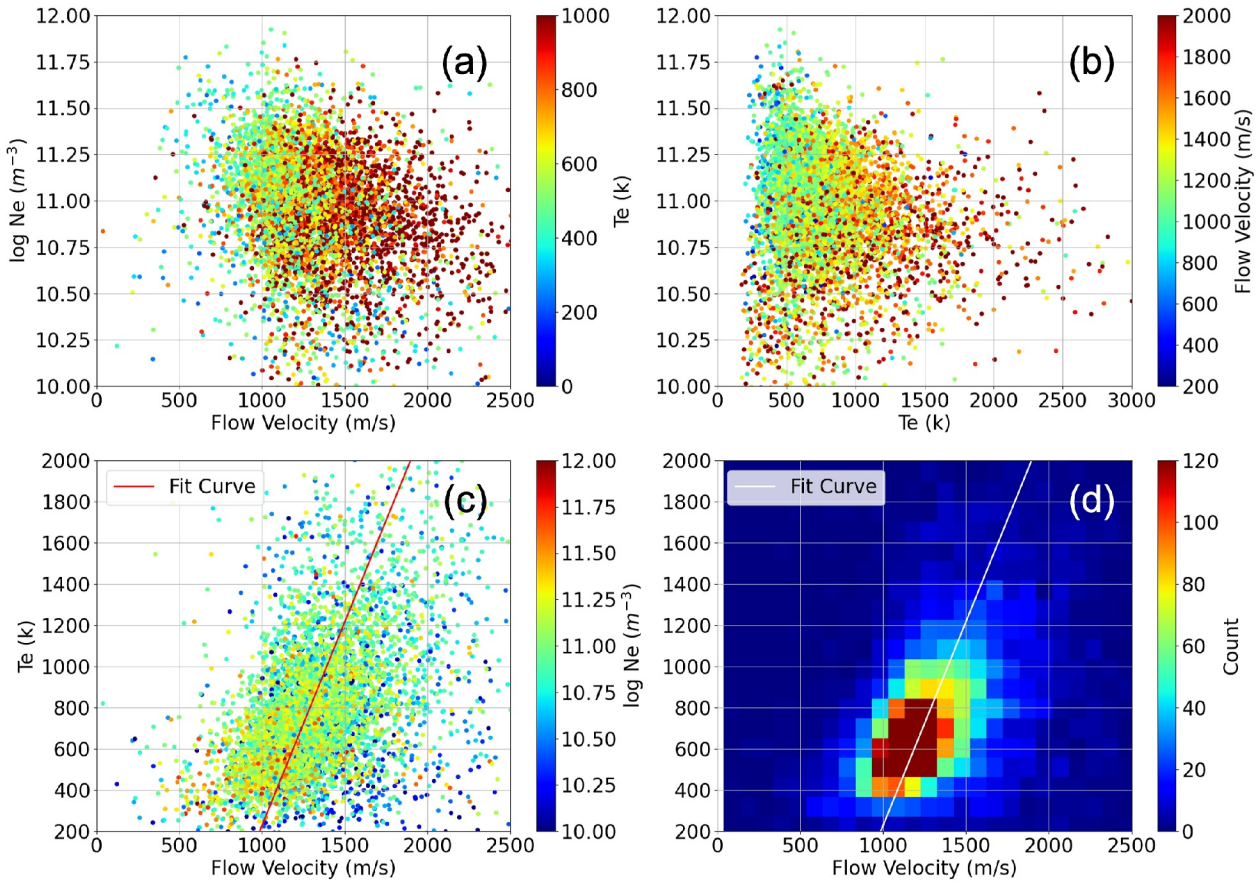

Figure 4. The representation of the AEH detection results in N-V-T space. Panel (a) displays the N-V scatter plot with color indicating electron temperature. Panel (b) illustrates the N-T scatter plot, where the color represents flow velocity. In panel (c), a T-V scatter plot is depicted with color mapping to electron density. Panel (d) presents a 2D histogram of the data in Panel (c). The red and white solid lines appearing in panels (c) and (d) are our linear fitting results.

According to the St-Maurice and Goodwin (2021) empirical formula of the T-V relationship, our new algorithm should only detect AEHs above 513 K. Nonetheless, our results seem to indicate that we are able to detect AEH events even below 500 K. This suggests that the actual electron temperature can be slightly lower than the one predicted by Equation 13.

The visualization of our fitting result is shown in Figure 5. The dashed blue line represents the St-Maurice and Goodwin (2021) empirical formula, and the solid blue line is our fit line. Initially, we divide the y-axis into small bins with a width of 50 K. We then employ the median value of flow velocity in each bin below 2100 K to generate a fit curve. This is because points above this temperature are sparse, and using those median values would induce significant deviation in the fitting result. The red points in Figure 5 represent the aforementioned median points used.

The fitting line indicates that the drift velocity where the predicted temperature exceeds 500 K is even higher than that proposed in the St-Maurice and Goodwin (2021) formula, escalating up to 1,150 m/s. Even accounting for the standard deviation of the electron temperature under the same electron density, this point remains larger than 1,000 m/s. Additionally, the slope of our fit line is steeper than that in the St-Maurice and Goodwin (2021) expression, implying that the electron temperature can escalate rapidly once the AEH is triggered. Simultaneously, in panel (b), the electron temperature seems to be lower than our fit curve when the flow velocity surpasses 2,000 m/s. This observation hints at a potential saturation effect at high flow velocities (Makarevich et al., 2013).

4.2. Occurrence Rate Trends

Figure 6 panel (a) showcases the distribution of AEH events over the years, juxtaposed with the long-term variance of the smoothed F10.7 solar radio flux index downloaded from the NOAA SWPC database. We have

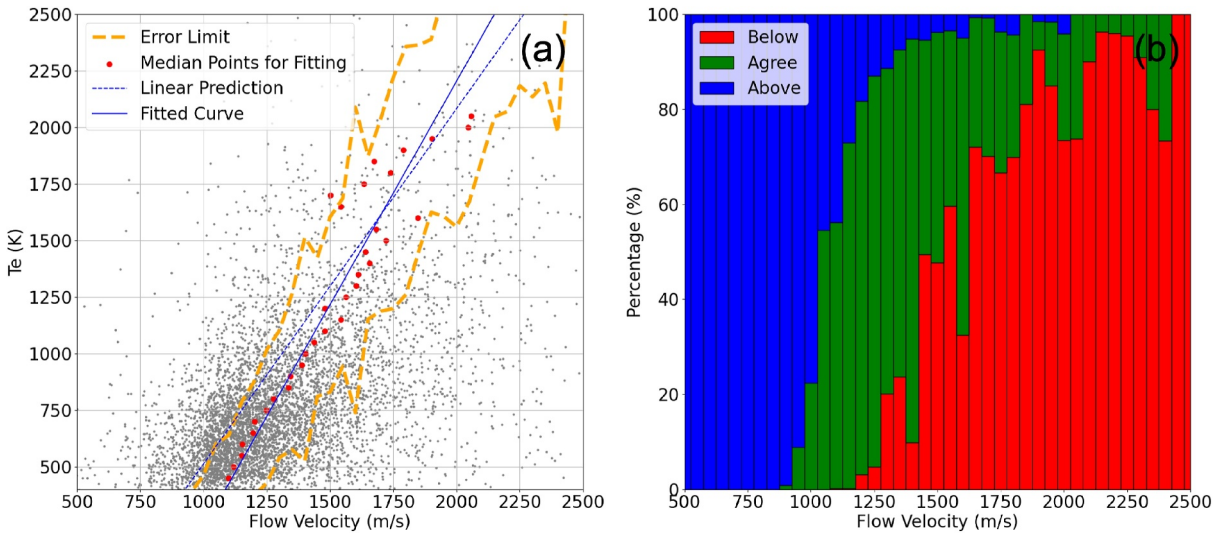

Figure 5. This figure illustrates our fitting process and results. In panel (a), the blue dashed line represents the St-Maurice and Goodwin (2021) empirical formula, the solid blue line is our fitting result, and the yellow dashed lines indicate the upper and lower limits of the fit considering the standard deviation, while the red dots signify the median flow velocity used for fitting. In panel (b), the blue bars represent the proportion of points above the fitting limits, the green bars show the proportion of points conforming to the fitting results, and the red bars depict the proportion of points below the fitting limits.

utilized AEH occurrence frequency rather than the count in order to avoid biases caused by substantial data gaps in 2014 and 2022. This frequency is derived by dividing the AEH count by the total duration covered with PFISR data. A discernible correlation between AEH occurrences and solar activity is evident from panel (a). The AEH occurrences hit the first peak in 2013 during the initial solar maximum of cycle 24 and align with the second, more pronounced solar maximum in 2015. Subsequently, the AEH occurrences undergo a gradual decline as we transition into a solar minimum. The frequency of AEH events sees a resurgence after the 2019 solar minimum, signaling the onset of a new solar maximum in cycle 25.

Panels (b) and (c) of Figure 6 compare AEH occurrence to the AE index. Due to data availability, we utilize the OMNI AE index through 2018 and the Proxy AE from the UCLA ELFIN database from 2019 to 2023. Panel (b) shows a scatter plot of the number of AEH events per 10 days against the average AE over 10 days. Panel (c) presents the same information as a 2-D histogram. Periods with frequent AEH also tend to be periods of elevated geomagnetic activity, as evidenced by the lack of points in the lower right corner of panel (b). The points in the upper left corner of panel (b) indicate that periods of elevated geomagnetic activity do not always correspond to observed AEH; however, this may be the result of the radar missing AEH events due to data gaps or periods where the radar is not at a favorable magnetic local time to observe AEH during a particular geomagnetic event. In conclusion, our statistical analysis underscores a robust correlation between AEH events, geomagnetic activity, and the solar cycle.

Figure 7 illustrates the distribution of AEH in season and magnetic local time (MLT). In concordance with the findings of Makarevich et al. (2013), our analysis reveals dual peaks in the AEH MLT distribution: one in the dusk sector at 17, and the other in the dawn sector, approximately at 4. A conspicuous asymmetry is evident between the two peaks, with a pronounced inclination towards the dusk sector. This pattern is similar to the statistical distribution of large flow velocities, so it is consistent with the relationship between AEH and fast flows. AEH is never observed at noon. PFISR is almost always equatorward of the auroral oval in the noon sector, and fast flows are not expected in the subauroral daytime ionosphere. Interestingly AEH is also very uncommon near midnight. The midnight sector is where the largest amounts of particle precipitation and auroral substorm activity is expected, so the lack of AEH in this sector indicates that AEH is not directly linked to substorms.

Furthermore, panel (b) indicates a higher likelihood of AEH events being detected in summer as opposed to winter. We are uncertain if this is a physical effect or a detection artifact. Incoherent scatter radar data has lower errors when the electron density levels are high, and therefore PFISR data is systematically better in summer than

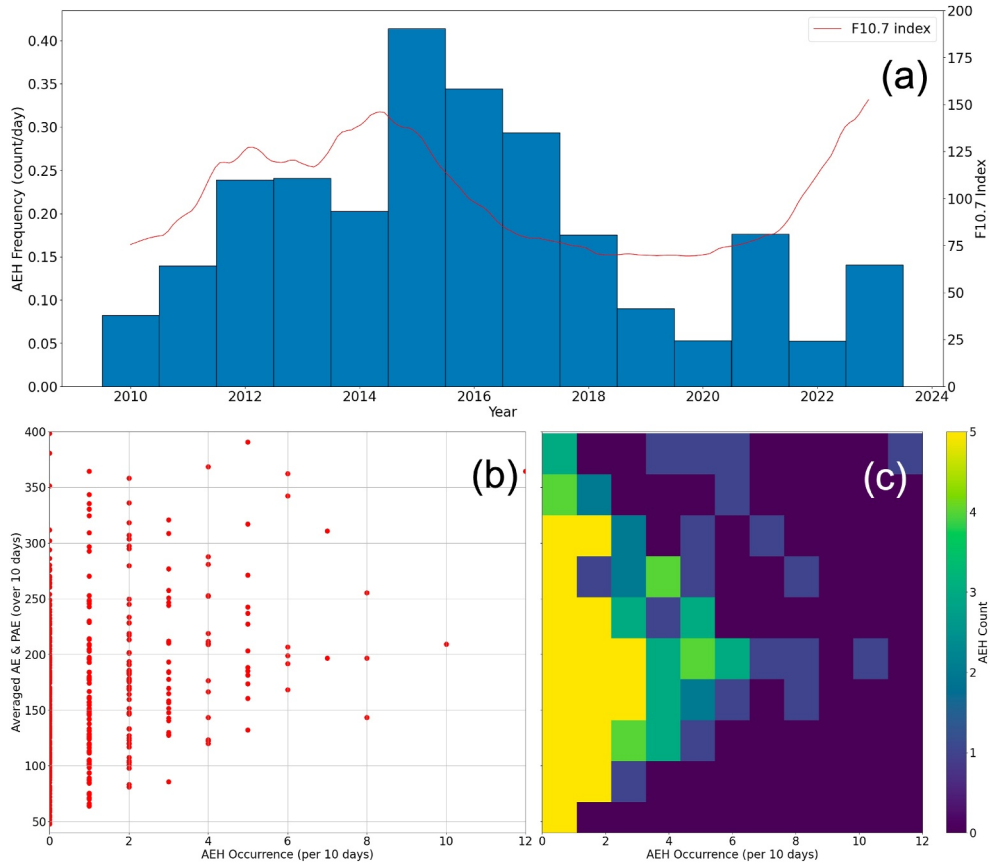

Figure 6. Relationships between AEH occurrence and space weather indices. Panel (a) compares the yearly AEH occurrence frequency (events per day) to the smoothed F10.7 index from OMNI. Panel (b) is a scatter plot of AEH occurrences per 10 days versus the average AE index over 10 days. Panel (c) is the same information presented as a 2-D histogram.

in winter. We may be more likely to detect AEH in summer simply because the summer data is normally higher quality than winter data.

5. Discussion

This study is the largest survey of AEH performed to date and the first to cover more than a complete 11-year solar cycle. In this section, we will first compare our statistical results with findings from earlier studies. Then, we will discuss the implications of our results for the theory of FBI and AEH.

5.1. A Comparison With Previous Findings

This work is a follow-on study to the first study by Makarevich et al. (2013). Makarevich et al. (2013) included conclusions on four aspects: the probability of AEH occurrence, the temporal distribution of AEH (magnetic local time, season), the linear relationship between plasma flow speed and electron temperature, and what he termed the "saturation effect."

As stated before, we designed an electron temperature based algorithm (labeled as algorithm 1 in Appendix A, Table A1), which is introduced in detail in Appendix A. This algorithm, which is very similar to the Makarevich et al. (2013) detection algorithm, detected 22 events in 2010 and 2011, which is the same number of events as detected by Makarevich et al. (2013) in that time period. Our events do not all match those in Makarevich et al. (2013) since we are using beam positions away from parallel to **B**, whereas Makarevich et al. (2013) analyzed the parallel to **B** beam (beamcode 64157). We had to avoid the parallel to **B** beam in our analysis to guarantee magnetic conjugacy with electric field measurements. Like Makarevich did in his work, we also manually went over all the detection results and visually confirmed that there are no false positives in our results.

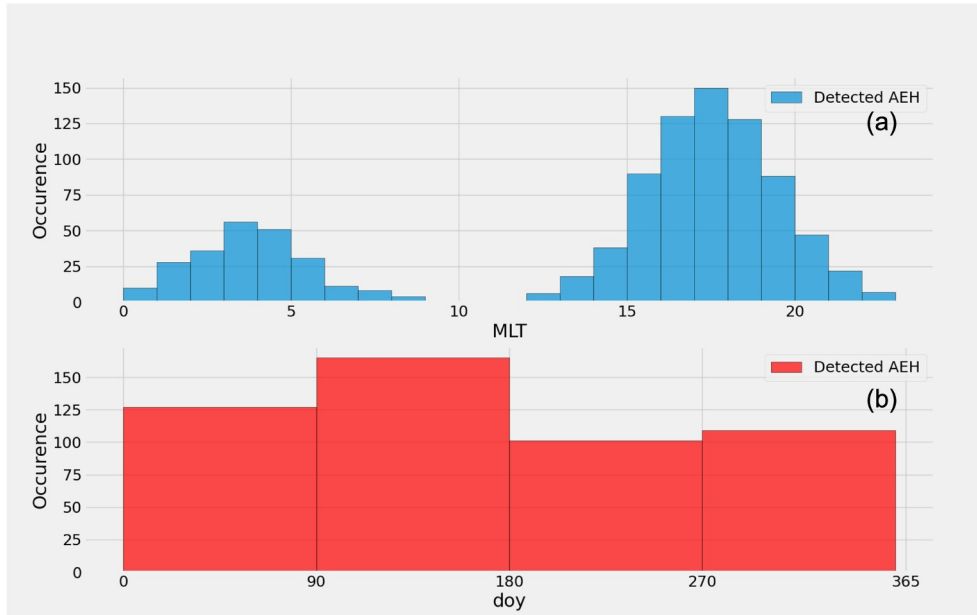

Figure 7. This figure displays the distribution of AEH events with respect to Magnetic Local Time (MLT) and season. Panel (a) illustrates the distribution of AEH events across different MLTs, while panel (b) showcases the distribution of AEH events throughout the various seasons.

Our more sensitive flow velocity based algorithm (labeled as algorithm 4 in Appendix A, Table A1) detects 48 events in 2010 and 2011, including a portion of weak and short events overlooked by the temperature-based algorithms.

Our AEH occurrence trends are consistent with the findings of Makarevich et al. (2013), which stated that the AEH occurrence rate increased from 0.12% to 0.27% in 2010 and 2011. We also found that the AEH occurrence rate nearly doubled between 2010 and 2011, from to 0.32%–0.51%, which is shown in panel (a), Figure 6. The summed data coverage we have in 2010 and 2011 is 487 (167 + 320) days. Using the Makarevich et al. (2013) occurrence rates, the total AEH time should be around 25.5 hr. This implies that the average expand of an AEH is 1.15 hr. This is consistent with our observation. Our calculation showed that the average span of an AEH in 2010 and 2011 is 1.08 hr.

Due to the use of a more comprehensive database, our distribution of AEH in magnetic local time, season, and year is smoother compared to the results of Makarevich et al. (2013). Overall, the magnetic local time distribution of AEH we obtained aligns with Makarevich's, both highlighting the bi-peak structure of AEH distribution and that AEH does not appear at midnight or noon. Given our larger data set (505 events to 22 events), our findings more clearly indicate the peak values of AEH's magnetic local time distribution to be at 17 and 3, a result that slightly differs from Makarevich's conclusion.

For the seasonal distribution, we examined 22 AEH events from 2010 to 2011 detected by algorithm 1. Indeed, as Makarevich et al. (2013) stated, there are more events in the spring and autumn seasons in those 22 events. However, based on the 48 results obtained from algorithm 4, the preference of AEH for spring and summer, especially for summer, becomes evident. For the 505 detected time intervals, the results are even more so, as shown in Figure 7.

By analyzing the flow velocities and electron temperatures of the 505 AEH events, we also observed a linear relationship between the two. The fitting results we obtained are consistent with those obtained by Makarevich. As is shown in Figure 5, when the flow speed is about 2,000 m/s, the electron temperature is 2000 K; and when the flow speed is about 1,200 m/s, the temperature is 800 K. However, because our fit took the median flow speed value within each electron temperature bin, the intercept on the horizontal axis is relatively large. Nonetheless, this does not affect the overall trend of the fitting results.

Our analysis indicates that $V_E > 1000$ m/s is an almost sufficient condition for the occurrence of AEH. However, this differs from the conclusions of Makarevich et al. (2013). They suggested that $V_E > 1000$ m/s is not a sufficient condition for AEH, because the times they observed $V_E > 1000$ m/s often did not fully coincide with the occurrence of AEH (usually slightly earlier or later). This is contrary to our observations; we found that $V_E > 1000$ m/s aligns very well with the time AEH occurs. After analysis, we believe the reason Makarevich arrived at such a conclusion is because the beam 64157 they used to observe electron temperature at 110 km reflects information at a geomagnetic latitude of 65.25°, while the electric field data was taken at 66° to avoid significant errors at 65.25°. This mismatch in measurement locations naturally led to the strong electric field not aligning well in time with AEH. In our analysis where we have carefully ensured magnetic conjugacy between our E-region temperature and F-region electric field measurements, the one-to-one correspondence between flows and temperature enhancements is much clearer.

We cannot use the current observations to directly confirm the saturation effect proposed by Makarevich et al. (2013). Even with 505 AEH events, we cannot determine whether a data point with an extremely high electric field value is a measurement error or a real electric field value. This is because we found that after 2019, PFISR often estimates extremely high electric fields accompanied by very abnormal data fluctuations. Such a situation is very likely due to errors in F-layer electron velocity measurements or electric field inversion. Therefore, we can only objectively state that our current observational data shows that the measured value is lower than the expected value in cases of extremely high electric fields.

5.2. Possible Suppression Mechanisms

Our results indicate that a positive growth rate from the linear fluid theory of FBI is not sufficient to predict the appearance of AEH. This indicates that either Farley-Buneman waves during moderate flow velocities (500–1,000 m/s) are too weak to generate detectable electron heating, or that the true threshold for FBI is higher than fluid theory predicts. Dimant et al. (2021) theorized the FBI should be suppressed in auroral arcs due to kinetic effects where energetic electron efficiently transfer energy between the waves and vibrational excitations of N_2, thereby damping the waves. Our analysis is not sufficient to prove this theory correct, but our results do show a lack of AEH events during times of high electron density.

A prominent feature in panels (a) and (b) in Figure A1 is the higher median electron density for the suppressed than for AEH events. The suppressed events in panel (b) have a median $\log_{10}N_e$ of 11.08, exceeding the typical density value at 110–120 km in the E-region, whereas the median for AEH events in panel (a) is 10.91. Furthermore, AEH is extremely rare when $\log_{10}N_e > 11.4$. This observation is further substantiated by the tilted slope of the SVM separation line discussed in Appendix A. Had the suppressed events not displayed a tendency to occur in high-density areas, the separation line would have been vertical instead of tilted.

Anecdotally we note a number of events like the right panels in Figure 2, where auroral arcs create high densities for extended periods, but the AEH only appears in a low density region between the auroral arcs. In this example the AEH event around 14 UT (3 MLT) appears during time of very low electron density. In this nighttime example, the very high electron densities at other times must have been created by auroral particle precipitation. No AEH is observed in the high density regions, despite the linear growth rate being positive ($OII > 1$) for most of the event.

The physical cause of the apparent suppression of AEH in high electron density regions remains unclear. One possibility is that high conductivity regions routinely short out electric fields, preventing sufficiently large electric fields from ever appearing colocated with high electron density. Another possible explanation is the Dimant et al. (2021) theory in which electrons at energies of several eV can suppress the FBI since those electrons have very high inelastic collision cross sections. Auroral particle precipitation produces a cascade of secondary electrons, filling phase space with electrons of the correct energies inside auroral arcs. In this theoretical picture high electron density does not cause suppression of the FBI directly, but high E-region electron density will be correlated with the presence of the several eV electrons that do suppress the instability since both are created by auroral particle precipitation.

Figure 8 compares the local time distributions of suppressed events (algorithm 2) and large AEH events (algorithm 1). In this figure "LT predicted AEH" refers to the sum of all events (algorithm 1 + algorithm 2), whereas "detected AEH" refers to algorithm 1. The distribution of all events above the threshold reflects the distribution of high flow velocities, and shows a clear two-peaked structure with peaks at dawn and dusk. Nonetheless, the

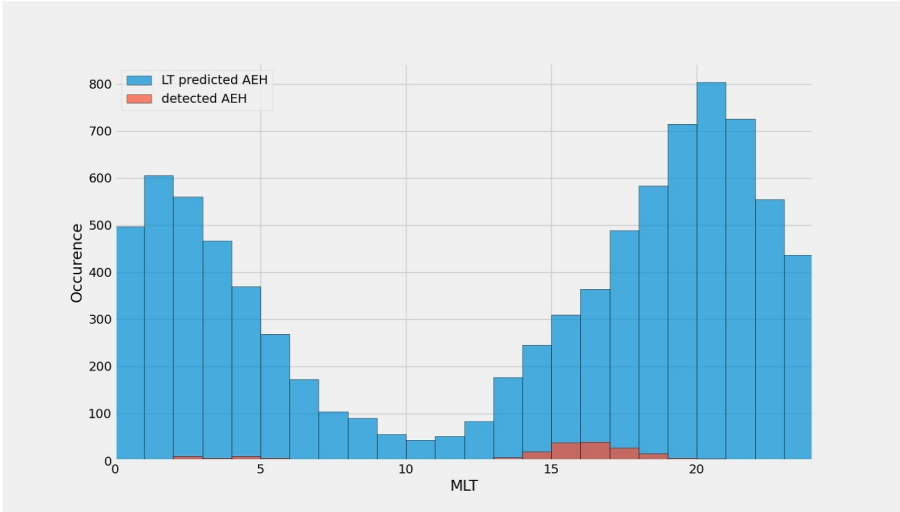

Figure 8. Histogram showcasing the distribution of AEH and suppressed events across Magnetic Local Time (MLT). The red bars represent the number of AEH events occurring within each MLT interval, while the blue bars denote the combined count of both suppressed events and AEH within the corresponding intervals.

locations of these peaks are not in the same places as the peak occurrence of AEH. Events above threshold are common between 20 and 2 MLT, but the AEH occurrence peaks in dusk sector at 16 MLT. This may be an effect of electron density and particle precipitation. Discrete auroral particle precipitation is very common in the midnight sector, and diffuse precipitation is common in the post-midnight sector. The preference for AEH in the dusk sector is consistent with AEH preferring periods of low electron density and low particle precipitation while also having large velocities.

6. Conclusions

We present a novel AEH detection algorithm for application to PFISR data. Our algorithm is primarily controlled by the flow velocities through our modified instability index. Our algorithm (algorithm 4) detects more events than a temperature-based algorithm with a high threshold (e.g. algorithm 1), but it does not suffer from as many false detections as a temperature-based algorithm with a low temperature threshold (e.g. algorithm 3). Application of our algorithm to 14-year of data (2010–2023) detects 505 events, with events being more common during times of elevated geomagnetic activity (high AE) and during solar maximum (high F10.7). This study is the first to quantify the solar cycle dependence of AEH since this study is the first to cover more than a full solar cycle of data. While AEH can appear at any point in the solar cycle, its frequency changes dramatically from a high of 0.4 events/day in 2015 to a low of 0.05 events/day in 2020. Our results also confirm a linear relationship between flow velocities and temperatures in AEH, which is consistent with prior studies.

An intriguing finding of our study is that most AEH is observed at velocities above 1,000 m/s, which is higher than the threshold for FBI predicted by linear theory. Indeed, a simple algorithm only based on checking for a positive growth rate of FBI will massively overestimate the true number of AEH events. This may indicate that Farley-Buneman waves with flows between 500 and 1,000 m/s are simply not strong enough to cause detectable electron heating, but it could also be the result of additional features of FBI theory not captured by fluid theory. Our results indicate that AEH systematically prefers periods of lower electron density and systematically prefers the dusk sector. These results are consistent with the theory of Dimant et al. (2021) that FBI should actually be suppressed in auroral arcs. Nonetheless, our results cannot directly confirm the theory Dimant et al. (2021) since we do not have direct measurements of the electron phase-space distributions needed to fully test the theory.

Appendix A: Development of the Modified Instability Index

This appendix explains how the separation value of 1,000 m/s was determined in the development of the modified instability index. Throughout our research process, we designed four different algorithms in total. As introduced

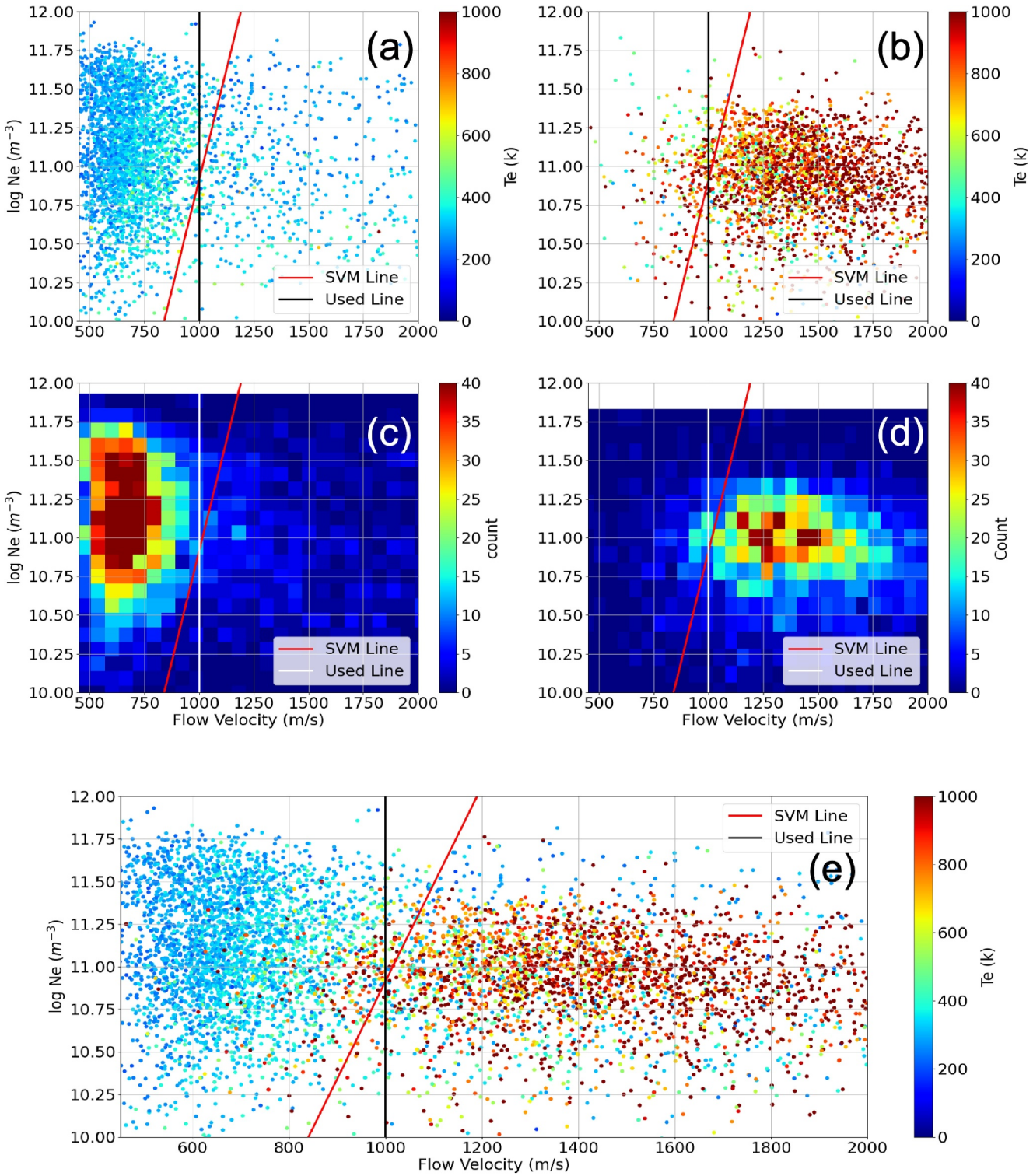

Figure A1. Illustration of the distribution of suppressed events and AEH detected by algorithm1 in N-V space, alongside their corresponding separation line. Panels (a and b) depict N-V scatter plots, where the color of each point represents temperature. Panels (c and d) display N-V 2D histograms, with the color of each bin representing the number of points it contains. The red line signifies the separation line obtained through SVM methods and the white and black lines indicating the separation line we actually use. Panel (e) encompasses both suppressed events and AEH.

Table A1
Anomalous Points Detection Criteria of All Algorithms

Algorithm	Anomaly point criteria
Algorithm 1	$T_e \geq 750$ and $OII \geq 0.75$
Algorithm 2	$T_e \leq 400$ and $OII \geq 1$
Algorithm 3	$T_e \geq 450$ and $OII \geq 1.1$
Algorithm 4	$T_e \geq 450$ and $MII \geq 1.1$

in Section 3.3, our algorithms can be separated into two parts. The first part involves identifying "anomaly data points" within data sets. The other part of the algorithm performs temporal correlation analysis on these anomaly data points. The anomaly points detection criteria of four algorithms are listed in Table A1. The final detection algorithm we used in the main text is numbered as "algorithm 4" in the table. Algorithm 1 is designed to detect the subset AEH events with especially high temperatures, but it will miss many AEH events with more moderate temperature enhancements. Algorithm 2 is designed to detect "suppressed events" where the instability threshold is exceeded but no elevated temperature is observed. Algorithm 3 detects events above the instability threshold, including many false positive events with no significant heating.

Our algorithm 1 is primarily sensitive to temperature and is therefore similar to the work of Makarevich et al. (2013). Nonetheless, this algorithm misses many AEH events with more moderate enhancements in the 400–750 K range. Our initial run of AEH detection utilizing algorithm 1 identified 240 AEH events from 2010 to 2023. While this algorithm yielded a minimal number of false positives, it notably overlooked many AEH events, as evidenced by the 505 events detected by algorithm 4, discussed in Section 3.4. This discrepancy primarily stems from the stringent electron temperature criteria, rendering the algorithm less responsive to shorter and weaker events. Lowering the temperature threshold captures more AEH events, but it also introduces a large number of false positives. Distinguishing AEHs from other events in this temperature range is difficult and time-consuming due to measurement errors and the presence of multiple heating mechanisms, such as Joule heating or precipitation heating.

We introduced the $OII > 1$ criterion based on the fluid instability threshold to attempt to reject these false positives. Nonetheless, we observed that the condition $OII > 1$ is frequently satisfied (approximately $V_E > 500$ m/s), particularly in the dawn, dusk, and night sectors. This implies a heightened likelihood of simultaneous occurrence of measurement errors electron temperature and $OII > 1$, thereby rendering the latter ineffective in eliminating false positives. The $OII > 1$ criterion is satisfied so frequently that algorithm 1 is primarily governed by temperature alone.

To detect a greater number of AEH events while minimizing false positives, it is imperative to devise a new strategy for detecting AEH events. Beyond electron temperature, plasma flow velocity and electron density are as two pivotal parameters to consider when detecting AEHs. Our goal for the new algorithm is to encapsulate the majority of the AEH events previously identified by algorithm 1, while simultaneously avoiding false positive results.

A1. Determination of the Separation Value

A portion of the false positives are "suppressed events" where the *OII* suggests the instability should exist, but no AEH is observed. In order to learn how to reject suppressed events, we developed algorithm 2 to detect suppressed events. In Table A1, the term "and" between two conditions signifies a logical AND, implying both conditions must be met. Our algorithm 2 is designed to detect low temperatures during times of positive instability growth rate, indicating suppression. The criterion was set to $T_e \leq 400$ and $OII > 1$.

Algorithm 1 detects clearly non-suppressed AEH events, and algorithm 2 detects clearly suppressed events. The distributions of electron density versus flow velocity for detected AEH and suppressed events are depicted in Figure A1. Panels (a) and (c) show plots of suppressed events (algorithm 2), while panels (b) and (d) show those of AEH events (algorithm 1). There are many more suppressed events than non-suppressed events. The points in

panel (a) represents the average value of a single event. For the points in panel (b) we did not average over events in time, but we did average over heights between 105 and 115 km.

A clear gap exists between two groups. We observe that the vast majority of points for suppressed events are clustered in the top left corner (high density, low velocity), whereas the points for AEH events are distributed across the remaining areas of the graph. This trend becomes even more pronounced in the 2D histogram, where a distinct separation line is evident between the two clusters of points. We determined an optimal separation line between the two classes of points using a Support Vector Machine (SVM), using the `scikit-learn` implementation of SVM (Pedregosa et al., 2011). SVM is an unsupervised machine learning algorithm extensively utilized for classification, regression, and outlier detection tasks. In classification problems—its most common application—the algorithm functions by identifying the hyperplane that best separates data points of different classes in the feature space. In this context, we input two groups of points with labels: points in suppressed events (algorithm 2) are labeled as group 0, while points in AEH events (algorithm 1) are labeled as group 1. The calculated separation line is represented by a tilted line exhibiting a steep slope, as depicted by the solid line in Figure A1. The equation for this optimal separation line is

$$\frac{0.007632\,\frac{E_\perp}{B}+6.9356}{1.3350}-\log_{10}(N_e)=0 \tag{A1}$$

This optimal separation line is nearly a vertical line at $v = 1000$ m/s (vertical black or white line in Figure A1), and so for simplicity we will use this vertical line in the modified instability index. The tilt of the optimal SVM line may or may not be physically meaningful. The tilt suggests that the velocity limit for suppression is slightly higher when the electron density is higher.

The modified instability index using the vertical separation line created an algorithm that meets our goals. Given that the majority of the detected AEH events (90%) are located on the right side of the line, while the suppressed events we aim to avoid are predominantly (83%) on the left, by excluding everything to the left of the separation line and retaining those on the right, we can conserve most of the previously detected AEH events while circumventing the false positives.

A2. A Comparison Between the New Algorithm and Two Electron Temperature Based Algorithms

In order to evaluate the performance of algorithm 4, we compare its results to a control group using the same temperature threshold and the OII instead of the MII. Algorithm 3 and algorithm 4 both use $T_e > 450$ K, but algorithm 3 uses $OII > 1.1$ whereas algorithm 4 uses $MII > 1.1$. Given that the $OII > 1$ condition is met frequently, algorithm 3 remains a detection algorithm primarily based on electron temperature.

The outcomes generated algorithms 3 and 4 are illustrated in Figure A2. Panels (a), (b), and (e) depict the electron temperature versus flow velocity (T-V) scatter plot, a 2D histogram, and the N-V scatter plot for algorithm 3, while panels (c), (d), and (f) represent those for algorithm 4. A comparison between Panels (a), (b) and Panels (c), (d) reveals that algorithm 3 exhibits greater detection errors in both electron temperature and flow velocity. Note that these plots show every point in a detected AEH events, not just the anomaly points exceeding the 450 K threshold. Some points in a continuous AEH event can be below the 450 K threshold so long as enough sequential data points exceed the threshold for the sequential analysis algorithm to classify it as an event. Similarly, there are some points in Figures 4 and A2 that fall below the set boundary ($V_E = 1000$ m/s) since the MII is used as the criterion to detect anomaly points, but a continuous event can fluctuate above and below the threshold due to measurement variations. Approximately 6% of the points in panels (a) and (b) fall below 400 K, the typical electron temperature value at 110 km. Moreover, a substantial variance observed at the high-temperature end of 1400–2000 K is likely caused by exceedingly large errors in temperature measurements or in electric field reconstruction.

Algorithm 3 contains many ambiguous events. Over a hundred points are categorized within the bin characterized by a flow velocity of 500–1,000 m/s and an electron temperature of 400–600 K. However, within these events, there is no apparent correlation between V and T. Their comparatively modest flow velocities imply that these events might have undergone heating through alternative mechanisms such as Joule heating, or they might be attributable to errors in temperature measurements during both AEH events and quiet times. After visually

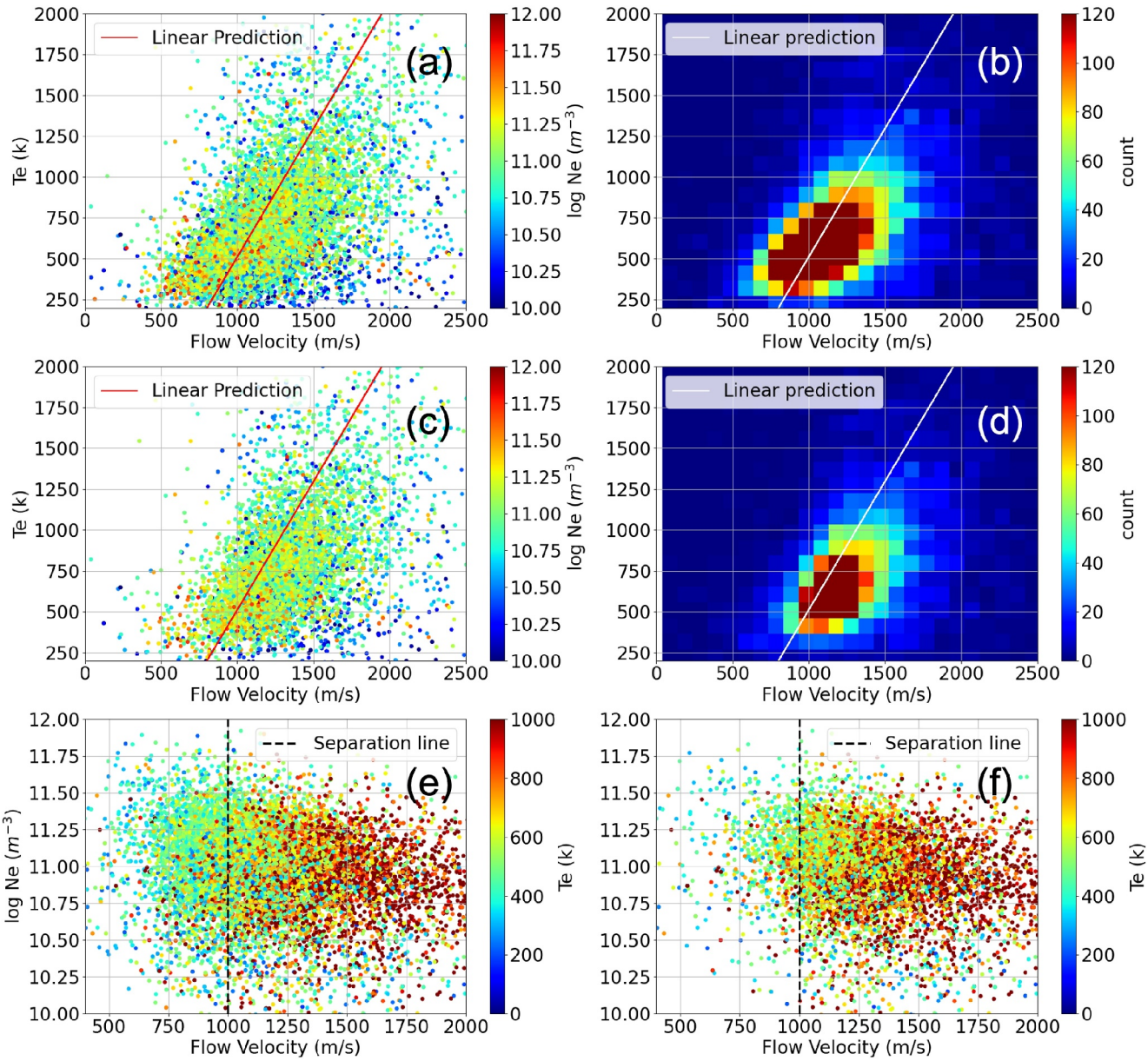

Figure A2. This figure presents a comparison between the detection results of algorithm 3 and algorithm 4. Panels (a, b, and e) depict the outcomes ascertained by algorithm 3, while panels (c, d, and f) showcase those of algorithm 4. Panels (a and c) illustrate T-V plots, where the coloration signifies electron density. The data points represented in these panels are averaged within a height range of 105–115 km during AEH events and have not been subjected to any further filtration. Panels (b and d) serve as histograms for panels (a and c) respectively. In panels (a) through (d), the red and white solid lines represent the St-Maurice and Goodwin (2021) T-V relationship at 110 km altitude. Panels (e and f) exhibit N-V distribution plots; herein, the black dashed lines denote the previously determined separation line, and the color of the points illustrates the electron temperature.

inspecting the measurements during these events, we found it challenging to definitively ascertain the heating mechanism. We did not want to include these ambiguous events in our statistical analysis of AEH occurrence. These results lead us to the conclusion that we ultimately cannot estimate the number of false positives contained within algorithm 3.

In contrast, panels (c) and (d), representing the results of algorithm 4 based on MII, feature very few points below the 400 K line. The count of points in the bin with flow velocities ranging from 1,000 to 1,500 m/s and electron temperatures below 400 K is notably lower than in panel (a). This subset of points is attributable to detection or measurement errors but exists on the right side of the suppression line. Consequently, the MII condition can

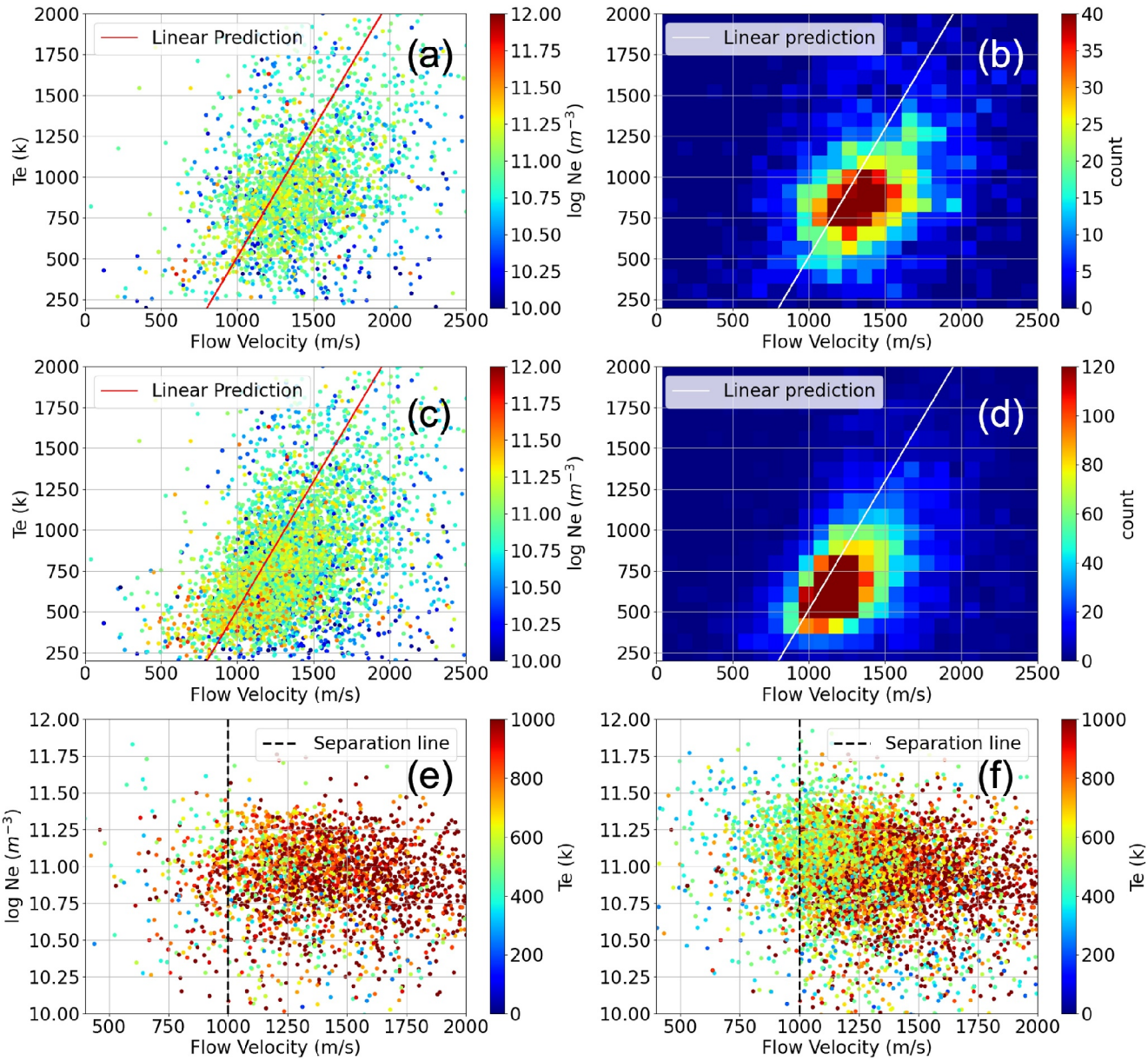

Figure A3. This figure presents a comparison between the detection results of algorithm 1 and algorithm 4. Panels (a, b, and e) depict the outcomes ascertained by algorithm 1, while panels (c, d, and f) showcase those of algorithm 4. Panels (a and c) illustrate T-V plots, where the coloration signifies electron density. The data points represented in these panels are averaged within a height range of 105–115 km during AEH events and have not been subjected to any further filtration. Panels (b and d) serve as histograms for panels (a and c) respectively. In panels (a) through (d), the red and white solid lines represent the St-Maurice and Goodwin (2021) T-V relationship at 110 km altitude. Panels (e and f) exhibit N-V distribution plots; herein, the black dashed lines denote the previously determined separation line, and the color of the points illustrates the electron temperature.

substantially mitigate errors on its right side, not just eliminating points on its left. Furthermore, the bulk of the points in panel (c) are visibly more clustered, indicating reduced errors in both dimensions. The elimination of error points at the high-temperature end results in a diminished variance in this region.

Focusing on the points exhibiting exceptionally high flow velocities within 2,000–2,500 m/s and temperatures below 1000 K, it is evident that panel (c) houses fewer points in this range compared to panel (a). Given the improbability of such strong electric fields with electron temperature lower than 1000 K, points within this range are highly likely to stem from errors in electric field measurements. Hence, a reduced number of points in this

range serves as direct evidence that employing MII yields fewer false positive results and errors compared to utilizing OII.

Due to the cut-off applied to the left of the separation line, over 90% of the points in this region are excluded. This substantial shift is illustrated in the final two panels. However, as previously noted, the separation line serves a dual purpose—it not only eliminates points to its left but also significantly reduces errors to its right. Therefore, we can deduce that algorithm 4 will produce fewer false positive results compared to algorithm 3.

Events in Figure 2 are two typical examples. They were both detected only by algorithm 4 but not by algorithm 1. In both cases, the electron temperatures are both around 500 K, and their temporal correlations are not that strong. But their electron temperature profiles and strong correlations between flow velocity and electron temperature suggest that theses two events are genuine AEH.

The more direct comparison between algorithm 1 and algorithm 4 is shown in Figure A3. First, due to the limited detection results of algorithm 1, the scatter plot of T-V obtained does not show a clear concentration around a linear trend, but rather scatters around the linear trend with significant deviations. Moreover, because of the overly high temperature threshold of algorithm 1, only a few points fall below 750 K. At the same time, ultra-strong AEH events above 1500 K only account for a small portion of the total number. As a result, as can be seen from panel a, the points in the T-V scatter plot obtained by algorithm 1 are mostly concentrated in a narrow temperature range, which does not show a good linear trend. In contrast, since algorithm 4 has many detection results in the range of 400–750 K, the linear relationship between T and V is more pronounced.

In conclusion, while reducing the temperature criterion in a temperature-based algorithm like algorithm 3 can enable the detection of weaker AEH events, the number of false positives and errors in the detection result will escalate to an unacceptable level. However, our algorithm 4, which primarily relies on the flow velocity, possesses the capability to detect weaker events without incurring an unacceptable and unpredictable number of detection errors. When fitting these points linearly, the results of algorithm 4 will yield better outcomes due to its wider temperature range, while the scatter of algorithm 1 cannot produce satisfactory results.

Furthermore, since the separation line derived by SVM also depends on electron density, another inference that can be drawn is that the actual threshold is intrinsically connected to electron density. This observation could also provide insight into the Dimant et al. (2021) theory on suppression by enhanced precipitation.

Data Availability Statement

PFISR data is available from the SRI International AMISR database (SRI International, 2023). Geophysical index AE was downloaded from the NASA OMNI data service (NASA, 2023) while index F10.7 was downloaded from the NOAA SWPC data service (NOAA SWPC, 2023). For 2019–2023, the Proxy AE data were downloaded from the UCLA ELFIN database (UCLA, 2023). The code required to generate the figures in this paper as well as complete tables of the detected events are available from Zhang and Varney (2024).

Acknowledgments
YZ was supported by a USTC Fellowship from the University of Science and Technology of China. RHV was supported by the National Science Foundation Faculty Development in Space Sciences award AGS-1936186. This material is based upon work supported by the Poker Flat Incoherent Scatter Radar which is a major facility funded by the National Science Foundation through cooperative agreement AGS-1840962 to SRI International.

References

Bahcivan, H., Hysell, D. L., Lummerzheim, D., Larsen, M. F., & Pfaff, R. F. (2006). Observations of colocated optical and radar aurora. *Journal of Geophysical Research*, *111*(A12), A12308. https://doi.org/10.1029/2006JA011923

Buneman, O. (1963). Excitation of field aligned sound waves by electron streams. *Physical Review Letters*, *10*(7), 285–287. https://doi.org/10.1103/PhysRevLett.10.285

Chapman, S. (1956). The electrical conductivity of the ionosphere: A review. *Il Nuovo Cimento*, *4*(4), 1385–1412. https://doi.org/10.1007/BF02746310

Dimant, Y. S., Khazanov, G. V., & Oppenheim, M. M. (2021). Effects of electron precipitation on E-region instabilities: Theoretical analysis. *Journal of Geophysical Research: Space Physics*, *126*(12), e2021JA029884. https://doi.org/10.1029/2021JA029884

Dimant, Y. S., & Milikh, G. M. (2003). Model of anomalous electron heating in the E region: 1. Basic theory. *Journal of Geophysical Research*, *108*(A9), 1350. https://doi.org/10.1029/2002JA009524

Dimant, Y. S., & Oppenheim, M. M. (2011a). Magnetosphere-ionosphere coupling through E region turbulence: 1. Energy budget. *Journal of Geophysical Research*, *116*(A9), A09303. https://doi.org/10.1029/2011JA016648

Dimant, Y. S., & Oppenheim, M. M. (2011b). Magnetosphere-ionosphere coupling through E region turbulence: 2. Anomalous conductivities and frictional heating. *Journal of Geophysical Research*, *116*(A9), A09304. https://doi.org/10.1029/2011JA016649

Farley, D. T., Jr. (1963). A plasma instability resulting in field-aligned irregularities in the ionosphere. *Journal of Geophysical Research*, *68*(22), 6083–6097. https://doi.org/10.1029/JZ068i022p06083

Heinselman, C. J., & Nicolls, M. J. (2008). A Bayesian approach to electric field and E-region neutral wind estimation with the poker flat advanced modular incoherent scatter radar. *Radio Science*, *43*(5). https://doi.org/10.1029/2007RS003805

Huuskonen, A., Lehtinen, M. S., & Pirttilä, J. (1996). Fractional lags in alternating codes: Improving incoherent scatter measurements by using lag estimates at noninteger multiples of baud length. *Radio Science*, *31*(2), 245–261. https://doi.org/10.1029/95RS03157

Huyghebaert, D., St.-Maurice, J.-P., McWilliams, K., Hussey, G., Howarth, A. D., Rutledge, P., & Erion, S. (2021). The properties of ICEBEAR E-region coherent radar echoes in the presence of near infrared auroral emissions, as measured by the Swarm-E fast auroral imager. *Journal of Geophysical Research: Space Physics*, *126*(12), e2021JA029857. https://doi.org/10.1029/2021JA029857

Kudeki, E., & Milla, M. A. (2011). Incoherent scatter spectral theories—Part I: A general framework and results for small magnetic aspect angles. *IEEE Transactions on Geoscience and Remote Sensing*, *49*(1), 315–328. https://doi.org/10.1109/TGRS.2010.2057252

Lehtinen, M. S., Huuskonen, A., & Markkanen, M. (1997). Randomization of alternating codes: Improving incoherent scatter measurements by reducing correlations of gated autocorrelation function estimates. *Radio Science*, *32*(6), 2271–2282. https://doi.org/10.1029/97RS02556

Liu, J., Wang, W., Oppenheim, M., Dimant, Y., Wiltberger, M., & Merkin, S. (2016). Anomalous electron heating effects on the E region ionosphere in TIEGCM. *Geophysical Research Letters*, *43*(6), 2351–2358. https://doi.org/10.1002/2016GL068010

Lotko, W., Smith, R. H., Zhang, B., Ouellette, J. E., Brambles, O. J., & Lyon, J. G. (2014). Ionospheric control of magnetotail reconnection. *Science*, *345*(6193), 184–187. https://doi.org/10.1126/science.1252907

Makarevich, R., Koustov, A., & Nicolls, M. (2013). Poker flat incoherent scatter radar observations of anomalous electron heating in the E region. *Annales Geophysicae*, *31*(7), 1163–1176. https://doi.org/10.5194/angeo-31-1163-2013

Merkin, V. G., Milikh, G., Papadopoulos, K., Lyon, J., Dimant, Y. S., Sharma, A. S., et al. (2005). Effect of anomalous electron heating on the transpolar potential in the LFM global MHD model. *Geophysical Research Letters*, *32*(22), L22101. https://doi.org/10.1029/2005GL023315

Milikh, G. M., Goncharenko, L. P., Dimant, Y. S., Thayer, J. P., & McCready, M. A. (2006). Anomalous electron heating and its effect on the electron density in the auroral electrojet. *Geophysical Research Letters*, *33*(13), L13809. https://doi.org/10.1029/2006GL026530

NASA. (2023). NASA OMNI data service [Dataset]. Retrieved from https://omniweb.gsfc.nasa.gov

NOAA SWPC. (2023). National oceanic and atmospheric administration space weather prediction center observed solar cycle indices [Dataset]. Retrieved from https://services.swpc.noaa.gov/json/solar-cycle/observed-solar-cycle-indices.json

Oppenheim, M. M., & Dimant, Y. S. (2013). Kinetic simulations of 3-D Farley-Buneman turbulence and anomalous electron heating. *Journal of Geophysical Research: Space Physics*, *118*(3), 1306–1318. https://doi.org/10.1002/jgra.50196

Pedregosa, F., Varoquaux, G., Gramfort, A., Michel, V., Thirion, B., Grisel, O., et al. (2011). Scikit-learn: Machine learning in Python. *Journal of Machine Learning Research*, *12*, 2825–2830.

Picone, J. M., Hedin, A. E., Drob, D. P., & Aikin, A. C. (2002). NRLMSISE-00 empirical model of the atmosphere: Statistical comparisons and scientific issues. *Journal of Geophysical Research*, *107*(A12), SIA15-1–SIA15-16. https://doi.org/10.1029/2002JA009430

Richards, P. G., Nicolls, M. J., Heinselman, C. J., Sojka, J. J., Holt, J. M., & Meier, R. R. (2009). Measured and modeled ionospheric densities, temperatures, and winds during the international polar year. *Journal of Geophysical Research*, *114*(A12), A12317. https://doi.org/10.1029/2009JA014625

Sahr, J. D., & Fejer, B. G. (1996). Auroral electrojet plasma irregularity theory and experiment: A critical review of present understanding and future directions. *Journal of Geophysical Research*, *101*(A12), 26893–26909. https://doi.org/10.1029/96JA02404

Saito, S., Buchert, S. C., Nozawa, S., & Fujii, R. (2001). Observation of isotropic electron temperature in the turbulent E region. *Annales Geophysicae*, *19*(1), 11–15. https://doi.org/10.5194/angeo-19-11-2001

Schlegel, K., & St.-Maurice, J. P. (1981). Anomalous heating of the polar E region by unstable plasma waves 1. Observations. *Journal of Geophysical Research*, *86*(A3), 1447–1452. https://doi.org/10.1029/JA086iA03p01447

Schunk, R. W., & Nagy, A. F. (2009). *Ionospheres: Physics, plasma physics, and chemistry* (2nd ed.). Cambridge University Press.

SRI International. (2023). SRI international AMISR database [Dataset]. Retrieved from https://data.amisr.com/

St-Maurice, J.-P., & Goodwin, L. (2021). Revisiting the behavior of the E-region electron temperature during strong electric field events at high latitudes. *Journal of Geophysical Research: Space Physics*, *126*(2), 2020JA028288. https://doi.org/10.1029/2020JA028288

St.-Maurice, J.-P., & Laher, R. (1985). Are observed broadband plasma wave amplitudes large enough to explain the enhanced electron temperatures of the high-latitude E region? *Journal of Geophysical Research*, *90*(A3), 2843–2850. https://doi.org/10.1029/JA090iA03p02843

St.-Maurice, J. P., Schlegel, K., & Banks, P. M. (1981). Anomalous heating of the polar E region by unstable plasma waves 2. Theory. *Journal of Geophysical Research*, *86*(A3), 1453–1462. https://doi.org/10.1029/JA086iA03p01453

UCLA. (2023). UCLA ELFIN proxy AE data [Dataset]. Retrieved from https://data.elfin.ucla.edu/proxy_ae/

Yamazaki, Y., & Maute, A. (2017). Sq and EEJ—A review on the daily variation of the geomagnetic field caused by ionospheric dynamo currents. *Space Science Reviews*, *206*(1), 299–405. https://doi.org/10.1007/s11214-016-0282-z

Zhang, Y., & Varney, R. H. (2024). Dataset for a statistical survey of E-region anomalous electron heating using poker flat incoherent scatter radar observations [Dataset]. https://doi.org/10.5281/zenodo.10341796